Design of halloysite-based nanocomposites by electrospinning for water treatment

Mahmoud Abid, Syreina Sayegh, Igor Iatsunskyi, Emerson Coy, Geoffroy Lesage, Arunas Ramanavicius, Abdesslem Ben Haj Amara, Mikhael Bechelany

Design of halloysite-based nanocomposites by electrospinning for water treatment

Mahmoud ABID [a,b], Syreina SAYEGH [a], Igor IATSUNSKYI [c], Emerson COY [c], Geoffroy LESAGE [a], Arunas RAMANAVICIUS[d,e], Abdesslem BEN HAJ AMARA [b,1] and Mikhael BECHELANY [a,*,1]

[a] Institut Européen des Membranes, IEM, UMR 5635, Univ Montpellier, ENSCM, CNRS, 34730 Montpellier, France

[b] Laboratory of Resources, Materials & Ecosystem (RME), University of Carthage, Faculty of Sciences of Bizerte, Zarzouna 7021, Tunisia
[c] NanoBioMedical Centre, Adam Mickiewicz University, Wszechnicy Piastowskiej 3, 61-614 Poznan, Poland
[d] Department of Physical Chemistry, Faculty of Chemistry and Geosciences, Institute of Chemistry, Vilnius University, Vilnius, Lithuania
[e] NanoTechnas – Center of Nanotechnology and Materials Science, Faculty of Chemistry and Geosciences, Institute of Chemistry, Vilnius University, Vilnius, Lithuania

_____

[*]Corresponding author
E-mail address: mikhael.bechelany@umontpellier.fr (M. Bechelany)
[1] Co-last authors

ABSTRACT

Titanium oxide (TiO_2) nanofibers are interesting for environmental applications, particularly solar energy and water treatment, due to their physical properties, chemical stability, high activity, and strong oxidation capacity. Here, we designed and synthesized halloysite-TiO_2 nanocomposite fibers by combining the electrospinning and sol-gel methods. Halloysite was extracted at Tamra (norther-western part of Tunisia). After optimizing the halloysite and TiO_2 ratio, we characterized the obtained hybrid materials by thermogravimetric analysis, X-ray diffraction, scanning and transmission electron microscopy, energy-dispersive X-ray spectroscopy, Raman spectroscopy, Brunauer-Emmett-Teller method, and X-ray photoelectron spectroscopy. The results confirmed halloysite incorporation into TiO_2 nanofibers. Moreover, when we used these halloysite-TiO_2 nanocomposite nanofibers as photocatalysts we found that >91% of methylene blue and acetaminophen was removed at neutral pH upon UV and visible light irradiation. Reusability tests showed good stability over five cycles under visible light. We also carried out acute toxicity and scavenging tests to monitor the formation of by-products and reactive species during acetaminophen degradation. We found that both $O_2^{\bullet-}$ and h^+ played a major role in its degradation. Overall, halloysite-TiO_2 nanocomposite nanofibers are effective catalysts for the removal of organic dyes and pharmaceutical compounds from water.

Keywords: halloysite nanotubes, TiO_2 nanofibers, electrospinning, photocatalysis, methylene blue, acetaminophen.

Graphical abstract

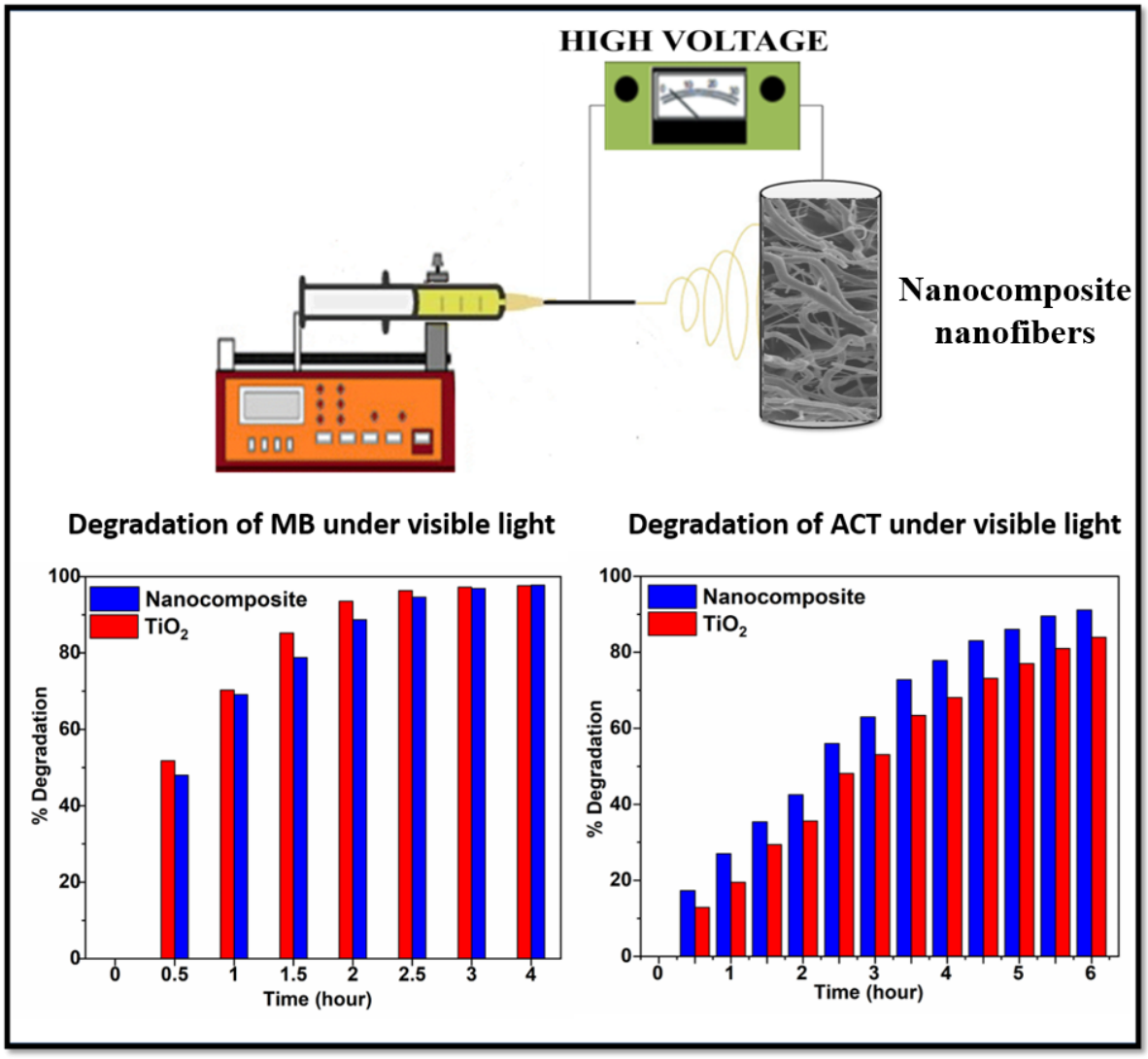

Highlights

1. **Composite nanofibers were prepared by combining halloysite and titanium oxide**
2. **These composite nanofibers were used for degrading acetaminophen and methylene blue under UV and visible light**
3. **Under visible light, >91% of acetaminophen and methylene blue was degraded after 150 and 360 min, respectively**
4. **The synthesized catalyst remained stable for five cycles.**
5. **The most active species involved in acetaminophen photodegradation were $^{\cdot}OH$, h^+ and $O_2^{\bullet-}$.**

1. Introduction

Worldwide, the drinking water reserves are decreasing as a consequence of the increase in water consumption and water pollution. The World Health Organization reported that safe drinking water and basic sanitation are not accessible to more than 2.2 billion people. Moreover, each year, diarrheal diseases, mainly caused by contaminated food/water, cause the death of more than 2.1 million people[1]. Water pollution is mainly due to the presence of dangerous chemical compounds (e.g. hydrocarbons, phenolic compounds, heavy metals, dyes, pharmaceuticals, insecticides)[2–7] that cannot be easily biodegraded and are often persistent in the environment.

Two strategies to eliminate these chemical pollutants from water sources have been mainly studied in the last years. The first approach is based on their storage on adsorbing materials, and the second approach focuses on their mineralization[8]. Adsorption on solid adsorbents remains the most used strategy[9] with good purification performances; however, its main drawback is the transfer of organic pollutants to the adsorbent, making its regeneration difficult and cost-ineffective[10]. Therefore, this method does not meet the current need of energy-friendly and low-cost treatment methods. On the other hand, advanced oxidation processes are environmentally friendly, less energy-demanding[11–13] and efficient methods for the degradation and mineralization of non-biodegradable molecules[14]. Among the existing advanced oxidation processes, heterogeneous photocatalysis is a promising alternative technology in the field of water and wastewater treatment[15,16].

In heterogeneous photocatalysis, the semiconductor material is activated by energy equal or greater than the semiconductor band gap. This leads to the excitation of electrons from the valence band to the conduction band and to the creation of electron-hole pairs that will create reactive species[17]. Because of their high oxidizing capacity, these radicals allow the mineralization of organic pollutants adsorbed on the surface of the photocatalyst and their transformation into H_2O, CO_2, and other mineral compounds (Cl^-, SO_4^{2-}, etc.)[18,19]. Most of the catalysts used for photodegradation are transition metal oxides that are classified in function of their stability, reactivity, and shape. Specifically, a good photocatalyst must remain stable over time to avoid efficiency loss[20]. Reactivity is influenced by the semiconductor features and the radical production kinetics. Solid catalysts can be used in the form of nanometric powders suspended or immobilized on a solid support.[21] In practice, titanium oxide (TiO_2), especially in the form of anatase, is considered the most promising semiconductor oxide on the basis of its good activity, and stability and low cost[22,23]. However, TiO_2 absorbs only a small fraction (3% - 5%) of sunlight (UV radiation) due to the anatase large band gap[24,25]. Other disadvantages are the poor TiO_2 recovery after water treatment and the fast recombination of the photogenerated charges.[26,27] Moreover, from an energetic point of view, a material with photocatalytic activity only under UV irradiation is not profitable. Therefore, it is important to develop economically interesting photocatalysts that can be activated by radiation in the visible spectrum, an ecological, abundant and free energy[28].

Efforts have been made to synthesize TiO_2 immobilized on an inert support (e.g. glass tubes, fibers, and stainless steel)[29]. However, this reduces the photocatalysis efficiency due to the lower specific surface area of the irradiated photocatalysts[30]. Some studies investigated the

use of porous materials (e.g. silica gel, zeolites and clays) as supports for pollutant adsorption[31–33]. Fibrous minerals (palygorskite[34,35], sepiolite[34–36] and halloysite[25–28]) are particularly interesting because of their pollutant adsorption and retention capacities and the possibility to modify their structures thanks to their cationic exchange properties and the presence of silanol groups [37]. Several studies showed that using halloysite (HNT) as support avoids TiO_2 agglomeration and allows producing adsorbents and catalysts with higher specific surface area.[38,39] Wang *et al.* prepared TiO_2/HNT samples with a Brunauer-Emmett-Teller (BET) surface area of 30.5 m^2/g for wastewater treatment using the solvothermal method. They reported higher photocatalytic degradation rates of methanol and acetic acid by the obtained nanocomposite (31.8 wt % TiO_2) compared with anatase [40]. Papoulis *et al.* produced anatase TiO_2 nanoparticles on HNT with a specific surface area of 187 m^2/g by hydrothermal treatment. This material showed higher activity in decomposing NO_x gas and toluene compared with commercial Titania P25 under UV and visible light irradiation [41]. Du *et al.* fabricated a TiO_2-HNT composite (TiO_2-HNT-300) using the sol-gel method and calcination and tested its photocatalytic activity against methylene blue (MB). After 4 h of UV irradiation, 81.6% of MB was degraded [42]. Zheng et al. synthesized an amylose-HNT-TiO_2 composite with high dispersion and large surface specific area (408.8 m^2/g) that effectively removed 91% of MB during 10 h of exposure to UV irradiation[43]. Moslehyani *et al.* described the preparation and characterization of electrospun nanofibrous adsorptive membranes with HNT-TiO_2 nanoparticles as adsorbents with a specific surface area of 17.9 m^2/g. These nanoparticles removed 31.2 mg/g arsenic from contaminated water[44]. Jiang *et al.* prepared TiO_2/HNT hybrid nanofibers by incorporating HNT by electrospinning. They found that the incorporation of 8% of HNT led to the best degradation performance (81% of MB after 90 min under visible irradiation). They explained this improved performance by the mass transport of reactant into the active nanofiber centers [45]. These studies indicate that the combination of TiO_2 and HNT is interesting for the efficient photocatalytic degradation of pollutants.

Here, a novel photocatalyst for removing dyes and pharmaceuticals from wastewater was developed using sol-gel processing with electrospinning and a large HNT amount (95%). HNT was extracted in Tunisia, purified, modified, and used for the development of a new porous hybrid material based on TiO_2 nanofibers by electrospinning. The structure and morphology of HNT, TiO_2, and the composite material were characterized by Fourier transform infrared spectroscopy (FT-IR), X-ray diffraction (XRD), scanning electron microscopy (SEM), energy dispersive X-ray (EDX), transmission electron microscopy (TEM), Raman and UV-Vis spectrophotometry. The new material was used for the degradation of MB and acetaminophen (ACT) under visible and UV light. The intermediates and reaction products from the photocatalytic degradation and the long-term catalytic stability were analyzed using high-performance liquid chromatography (HPLC). A toxicity screening test was used to characterize the acute toxicity of sub-products formed during ACT degradation. Scavenger tests were also performed to investigate the reactive species responsible for ACT degradation.

2. Materials and Methods

2.1. Materials

HNT was extracted from Tamra (Nefza District, in the North-West part of Tunisia) and purified by sedimentation and sodium exchange modification. Titanium tetraisopropoxide (TTIP, 97%,

CAS: 546-68-9), polyvinyl pyrrolidone (PVP, Mw=1300000, CAS: 9003-39-8), sodium chloride (NaCl, ≥99%, CAS: 7647-14-5), silver nitrate ($AgNO_3$, >99%, CAS: 7761-88-8), MB hydrate (CAS:122965-43-9), Nafion™ perfluorinated resin solution (CAS: 31175-20-9), ACT (≥99 % CAS: 103-90-2), 2-propanol (99.9%, CAS: 67-63-0), p-benzoquinone ($C_6H_4O_2$, ≥99.5%, CAS:106-51-4) and ethylenediaminetetraacetic acid (EDTA, 99.995%, CAS: 60-00-4) were from Sigma–Aldrich. Acetic acid (CAS: 64-19-7) and ethanol (≥99.8%, CAS: 64-17-5) were purchased from VWR chemicals and used as solvents. All chemicals were used without further purification. For the preparation of solutions and reagents, deionized water (>18.2 MΩ) produced with a Millipore (Milli-Q® Academic) water purification system was used.

2.2. HNT purification

Natural HNT was dispersed in deionized water and left overnight, then the fraction with a diameter >2 µm was removed by sedimentation [46]. The obtained clay was washed five times with deionized water and NaCl and separated by centrifugation. Na^+ HNT was then washed with distilled water and centrifuged six times until the test in the presence of $AgNO_3$ was negative. Purified HNT was dried in an oven at 110°C for 3 hours, crushed, and sieved.

2.3. Preparation of TiO_2 and HNT-TiO_2 (H95T5) nanofibers

To prepare the polymeric solution, 10% PVP was added to ethanol. Then, a TiO_2 solution was prepared by hydrolyzing TTIP with a mixture of ethanol and acetic acid (3:2:2). After mixing for 2h, the solution was loaded into a 20 mL plastic syringe and electrospun using a homemade electrospinning system and the parameters described in our previous work[47,48]. The as-spun TiO_2 nanofibers were left in the air to fully hydrolyze overnight, and then were calcinated in a furnace at 400°C with a heating rate of 1°C/min for 4 h to remove the polymer and achieve the desired crystallinity.

H95T5 nanofibers were prepared using a similar method, with the addition of HNT to the TiO_2 mixture (weight ratio 95:5) followed by sonication for 30 min. This specific ratio was the optimum ratio according to preliminary results (**Fig. S1**).

2.4. Structural characterization

Thermal analysis was performed at a heating rate of 20°C/min under airflow from room temperature to 1000°C using the SDT Q600 thermal analyzer (TA Instruments). The microstructure, phase, and crystal structure of the synthesized nanofibers were investigated by SEM (Hitachi S-4800) and TEM (JEOL 2200FS, 200 kV, Japan) with an EDX analyzer. The BET method, with different data points and relative pressures (P/Po) from 0 to 1, was used to describe the surface and micropore areas. The structural and crystallinity properties were studied by XRD (PANAlytical Xpert-PRO diffractometer equipped with a X'celerator detector using Ni-filtered Cu-radiation) and Raman spectrophotometry (Horiba Xplora, 532 nm). To determine the elemental composition and the oxidation states, X-ray photoelectron spectroscopy (XPS) was performed with an ESCALAB 250 spectrometer (Thermo Electron) and an Al Kα monochromatic source (1486.6 eV) as excitation source.

2.5. Electrochemical activity

For film deposition onto ITO glass (60 mm x 21mm x 2 mm), 5 mg catalyst was dissolved in a mixture of 1 mL isopropanol and 40 µL Nafion™, followed by sonication for 30 min. The slurry was deposited (coverage of 4 cm^2), dried at room temperature, and used as electrode.

Electrochemical impedance spectroscopy (EIS) was carried out using a Solartron SI 1287 galvanostat-potentiostat and a three-electrode system (Ag/AgCl as reference electrode, platinum wire as counter electrode, with 0.1M Na_2SO_4 as the electrolyte) in the dark and under visible light using a 150 W linear halogen lamp (the visible light source is in the 420–600 nm range). The distance between the lamp and the quartz window was maintained at 10 cm where the power density was 8.2 mW/cm^2. Electrochemical measurements were performed at room temperature and recorded at 0.4-0.6V [49].

2.6. Photocatalytic activity

The photocatalytic activity of HNT-TiO_2 composite nanofibers was evaluated by monitoring MB degradation under a medium pressure metal halide UV lamp (400 W, Lampes France) and a visible light source provided by a linear halogen lamp (400W, Avide). Briefly, 0.5 g/L of each photocatalyst was added to 250 mL of MB aqueous suspension (2.10^{-5} mol/L). Before irradiation with visible and UV light, nanofibers were dispersed in the solution by sonication in the dark for 30 min to reach the adsorption-desorption equilibrium. The distance between the lamp and the solution was fixed at 10 cm for all experiments, and the temperature was kept constant at 25°C by circulating water in the cylindrical tube surrounding the photo-reactor. At a specific time point (30 min for visible light and 10 min for UV), an aliquot of 2 ml was taken from each sample and centrifuged at 6000 rpm for 2 min in the dark to clear the supernatant.

The previous experiment was repeated by replacing MB with ACT (10ppm), without centrifugation. Aliquots were collected at different time points during the experiment and filtered through 0.45 µm filters. They were used to identify intermediates and reaction productions using a HPLC system equipped with a C-18 column (RP18, Nucleoshell) and a Quattro-Micro mass spectrometer with an electrospray probe (Waters Micromass, Wythenshawe, Manchester, UK) as detector.

The photocatalytic efficiency of the prepared nanocomposites was calculated using equation 1 [50]:

$$\text{Degradation efficiency (\%)} = [(C_0\text{-}C)/C_0]\text{x}100 \qquad (1)$$

where C_0 and C are the pollutant concentrations before and after photo-irradiation, respectively. This equation gives the percentage of pollutant degradation during the photocatalysis experiment.

2.7. Kinetic measurement

MB and ACT photocatalytic degradation kinetics under UV and visible light were investigated and the obtained data were fitted by a pseudo-first-order kinetic model described by equation *2* [51]:

$$\ln (C_0/C) = K_{app}\, t \qquad (2)$$

where C_o is the initial concentration, C the concentration at the time t, and K_{app} is the apparent rate constant.

2.8. Bacterial toxicity tests

To assess the solution toxicity during ACT photodegradation, bacterial toxicity tests were carried out using the bioluminescent marine bacterium *Vibrio fischeri*. All samples collected at different time points were diluted to 81.9% by adding 22% of NaCl solution to allow the bacterial activity and luminescence emission. The solution pH was fixed at 7, and samples were filtered through 0.45 µm syringe filters. Toxicity was expressed as the luminescence inhibition rate, measured with a Microtox 500 Analyzer, and calculated with equation 3 [52]:

$$Ic_{(t)}\,(\%) = \left(1 - \frac{LU_{(t)}}{LU_0 \text{ x } R_{(t)}}\right) \text{x}100 \qquad (3)$$

where $LU_{(t)}$ is the intensity of the luminescence emitted by bacteria after t = 15 min of contact with the sample, LU_0 is the initial bacterial luminescence intensity before addition of the sample, and $R_{(t)}$ is the corrected term. Indeed, in the absence of toxicity, the bacterial luminescence decreases over time under the influence of environmental conditions. Therefore, the natural luminescence variability must be taken into account to avoid errors. The corrected term is given by the following equation:

$$R_{(t)}\,(\%) = \left(\frac{LU_{0(t)}}{LU_0}\right) \text{x}100 \qquad (4)$$

where $LU_{0(t)}$ is the intensity of the luminescence emitted by bacteria after t = 15 min of contact with the control solution (deionized water and NaCl).

3. Results and Discussion

3.1. Morphological and structural characterization

The HNT-TiO_2 nanocomposite fibers synthesized by combining the electrospinning and sol-gel methods followed by calcination at 400°C under air were structurally and morphologically characterized. The plots of the thermogravimetric analysis of TiO_2, H95T5, and natural HNT **(Fig. S2)** indicated a multistage decomposition with relatively stable intermediate products, and confirmed that the H95T5 curve was a combination of the HNT and TiO_2 curves. The morphological analysis of HNT, TiO_2, and H95T5 nanotubes by SEM **(Fig. 1.a)** showed tubular structures with cylindrical and prismatic HNT with a diameter between 50 and 70 nm. TiO_2 fibers were uniform, continuous, randomly oriented, with a smooth surface, and a diameter between 200 and 300 nm **(Fig. 1.b)**. The hybrid nanofibers (H95T5) had a diameter ranging from 200 to 300 nm and retained the uniform morphology of TiO_2 fibers, with some spindle-shaped HNT aggregates that protruded from the hybrid nanofibers, probably due to the high HNT concentration in the sol-gel solution **(Fig. 1.c)**. This also confirmed that the moderate amount of TiO_2 was uniformly distributed in the H95T5 hybrids, as previously reported [39,40,53–61].

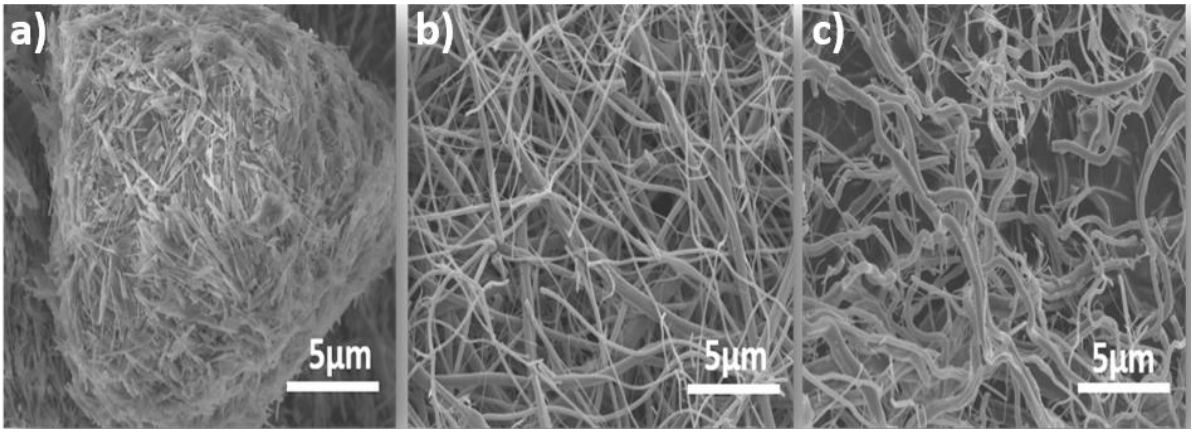

Fig. 1 SEM micrographs showing HNT fibers (a), TiO_2 nanofibers (b), and H95T5 nanocomposite fibers (c).

To study the sample crystallinity, XRD analysis were carried out. The XRD patterns of HNT, TiO_2 and H95T5 fibers at 2θ (**Fig. 2.a**) were characterized by a relatively sharp peak at 12.32°, which was the characteristic (001) reflection of HNT (7.18 Å), and by another reflection at 19.92°, which corresponded to the (110) plane. The next reflection at 24.51° corresponded to the (002) plane. Other reflections at 45.19° (123), 56.55° (114), and 62.22° (-331) were observed at 2θ [38,62]. Besides HNT, minerals, such as kaolinite, also were found at 2θ, as indicated by the reflections at 34.9° (-122), 35.87° (200), and 38.33° (1-31). The Bragg diffraction reflections of TiO_2, defined as 101, 112, 200, 105, 211, 204, 116, 220, and 215, corresponded to the TiO_2 anatase phase with a tetragonal arrangement[63,64]. The XRD patterns of H95T5 samples showed the presence of both HNT and anatase (**Fig. 2.a,** blue curve)[39,61,65].

The various functional groups present in the HNT, TiO_2, and H95T5 nanofibers were confirmed by FT-IR spectroscopy **(Fig. 2.b)**. In the HNT spectra, the two peaks at 3694 and 3617 cm^{-1} and the band at 907 cm^{-1} were assigned to the stretching vibrations of inner surface hydroxyl groups, and to the deformation vibration of inner surface hydroxyl groups, respectively. The peak at 528 cm^{-1} and the band at 455 cm^{-1} were attributed to the deformation vibration of Al-O-Si and to the stretching vibrations of Si–O–Si, respectively[41,65]. In the TiO_2 and H95T5 spectra, the characteristic band at 435 cm^{-1} corresponded to Ti–O-Ti vibrations [61]. The HNT bands related to hydroxyl groups, Al-O-Si and Si-O-Si were also observed in the H95T5 spectrum [39,66].

The Raman lines of HNT were broad and weak (**Fig. 2.c**) [67,68]. Conversely, the Raman spectra of TiO_2 and H95T5 (recorded from 50 to 800 cm^{-1}) allowed identifying the crystal phases of TiO_2[69] (**Fig. 2.d**). The crystalline anatase had a tetragonal space group D_{4h} ($I4_1$ /amd) and presented six Raman active modes (A_{1g}, 2 B_{1g}, 3Eg). These active modes occurred at ~142 cm^{-1} (Eg), 196 cm^{-1} (Eg), 390 cm^{-1} (B_{1g}), 511 cm^{-1} (A_{1g}), 512 cm^{-1} (B_{1g}), and 632 (Eg). Thus, the Raman spectroscopy data were in good agreement with the XRD and FTIR findings.

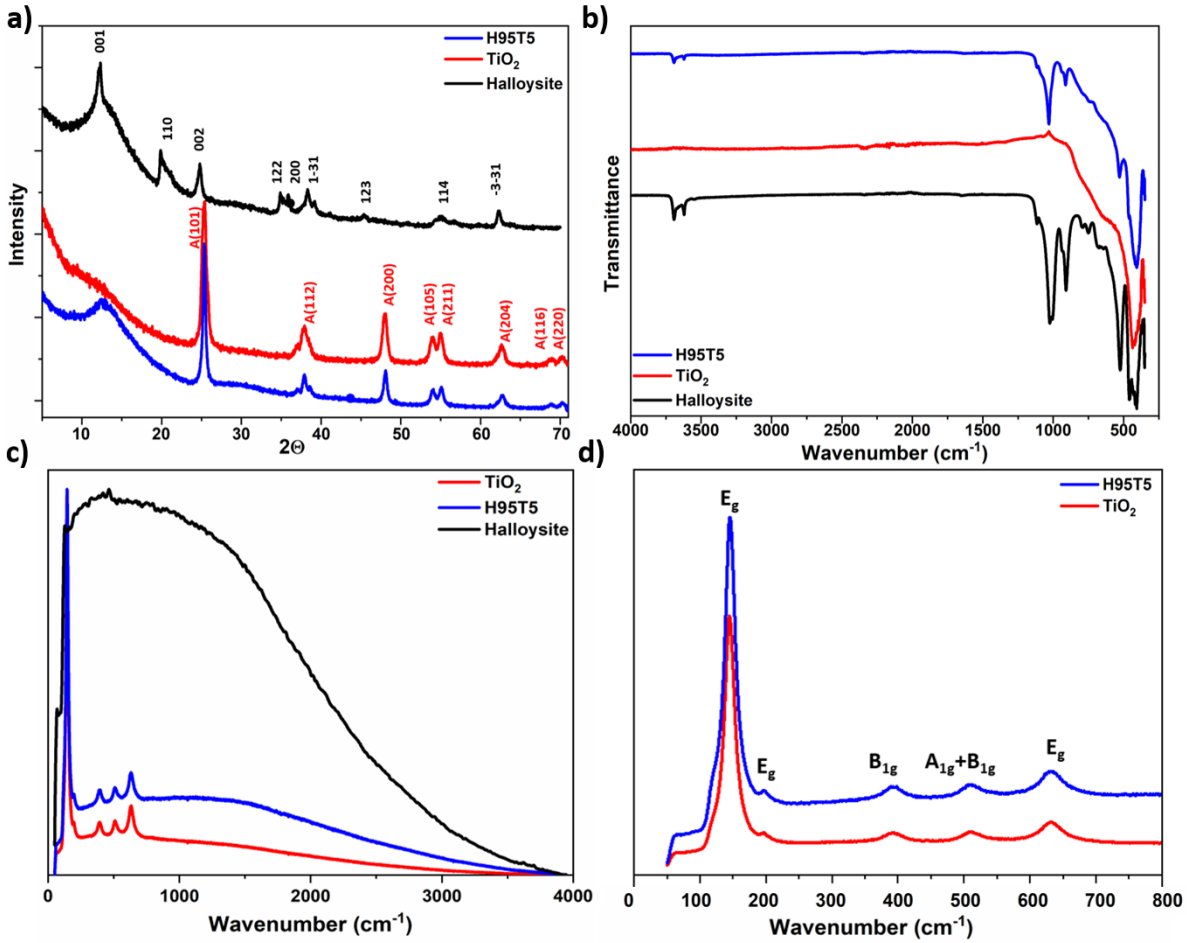

Fig. 2 XRD patterns (a), FT-IR spectra (b), and Raman spectra (c,d) of TiO_2, HNT, and H95T5 nanofibers.

To obtain more structural information, TEM analysis was performed. HNT displayed a nanotubular structure with an inner lumen **(Fig. 3.a and d)**[45]. TiO_2 nanofibers **(Fig. 3.b and e)** showed a rough and large surface [57,61]. The surfaces of H95T5 nanofibers and TiO_2 nanofibers were similar (compare **Fig. 3.b and c**). TEM analysis also indicated (**Fig. 3.c and f**) that HNT nanotubes were located inside the TiO_2 nanofibers[39,45]. Chemical mapping of H95T5 by scanning TEM (STEM) highlighted the homogenous distribution of Ti, Si and Al atoms (**Fig. 3.h**) Al–K and Si-K were inside the hollow nanofibers. These results strongly indicate HNT penetration inside the TiO_2 nanofibers [45,70,71].

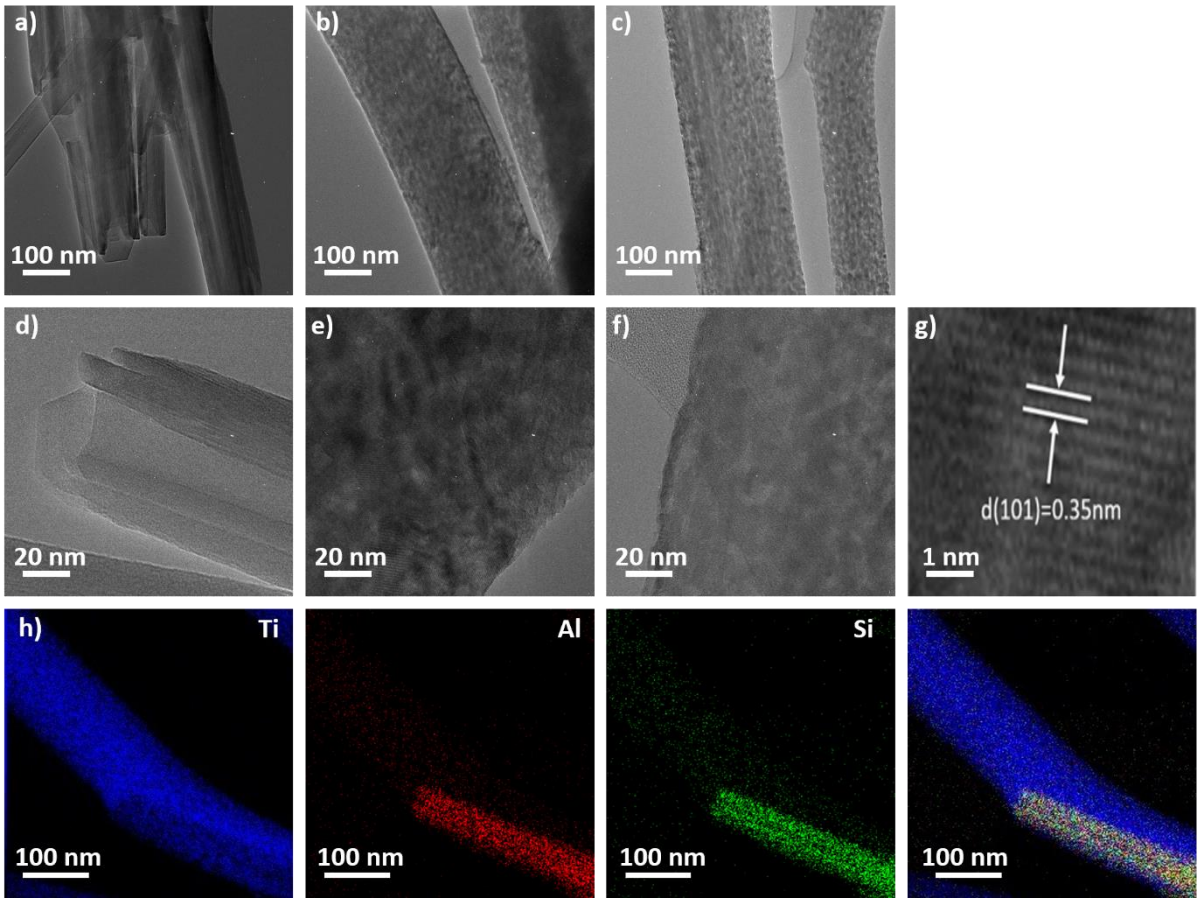

Fig. 3 TEM images of HNT (a,d), TiO_2 (b,e) and H95T5 (c,d), TEM image of TiO_2 (g), and STEM-EDX chemical mapping of H95T5 (h).

XPS was carried out to determine the surface structure and chemical state of each element. The deconvoluted spectra of Ti 2p, O 1s, C 1s, Al 2p and Si 2p are shown in **Fig. 4, Fig. S3** and **Fig. S4**, and summarized in **Table 1**. The Ti 2p spectrum of TiO_2 consisted of distinct Ti $2p_{1/2}$ and Ti $2p_{3/2}$ photoelectron signals that were located at 464.2 and 458.5 eV with a spin-orbital splitting of 5.7 eV[38,72]. In H95T5, Ti $2p_{1/2}$ slightly shifted toward lower binding energy (-0.4 eV) due to HNT presence[73]. In the O 1s region of H95T5, the binding energy value at 529.7 eV corresponded to the typical Ti-O-Ti peak[71]. The other peak at 531.1 eV was ascribed to O-Si shifting toward lower binding energy (-0.2 eV), compared with HNT, due to TiO_2 incorporation[73]. HNT displayed a H_2O signal at 533.5 eV. Si 2p peak deconvolution revealed the presence of only one peak with binding energy at 103.1 eV in HNT. This peak shifted toward lower binding energy (-0.6 eV) in the H95T5 spectra, indicating the presence of SiO_2 bonds. The Al 2p signal observed at 74.8 eV (HNT) and 74. 5 eV (H95T5) demonstrated the presence of Al^{3+}.

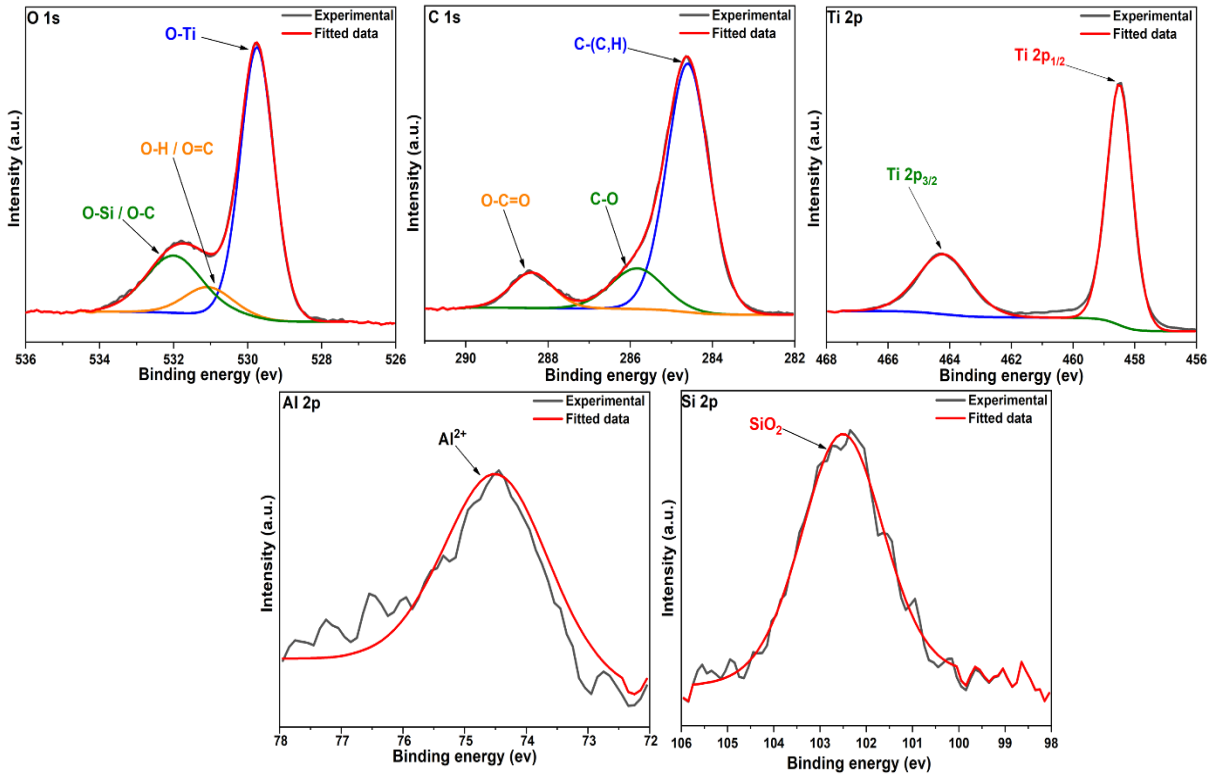

Fig. 4 Deconvolution of high-resolution XPS spectra for the elements in H95T5.

Table 1. Deconvoluted peaks of the XPS spectra.

Halloysite	**Position**	**TiO_2**	**Position**	**H95T5**	**Position**
O 1s O-H O-Al	531.2	O 1s O-Ti	529.7	O 1s O-Ti	529.7
O 1s O-Si O-C	532.2	O 1s O-H O=C	531.1	O 1s O-H O=C	531.1
O 1s H_2O	533.5	O 1s O-C	532.0	O 1s O-Si O-C	532.0
		Ti $2p_{3/2}$ TiO_2	458.5	Ti $2p_{3/2}$ TiO_2	458.5
		Ti $2p_{1/2}$ TiO_2	464.6	Ti $2p_{1/2}$ TiO_2	464.2
C 1s C-(C,H)	284.6	C 1s C-(C,H)	284.6	C 1s C-(C,H)	284.6
C 1s C-O	285.9	C 1s C-O	286	C 1s C-O	285.8
C 1s O-C=O	288.6	C 1s O-C=O	288.4	C 1s O-C=O	288.4
Si 2p SiO_2	103.1			Si 2p SiO_2	102.5
Al 2p (+III)	74.8			Al 2p (+III)	74.4

N_2 adsorption and desorption analyses were performed to investigate the surface and micropore area of HNT, TiO_2, and H95T5. The isotherm shapes of all samples (**Fig. S5**) belonged to the type IV (IUPAC classification) with a distinct type H_3 hysteresis loop at a relative pressure range of (0.7–1.0) for HNT and H95T5 and of (0.4-0.9) for TiO_2. This indicated that their mesoporous and microporous structures were preserved [74–80].

The BET surface and micropore area of as-prepared H95T5, TiO_2 and HNT nanocomposites (**Table 2**) indicated that the specific surface area of TiO_2 was 58.4 m^2/g, whereas those of HNT and H95T5 were very similar (35.7 and 36.6 m^2/g, respectively). This was mainly due to the high HNT percentage in the H95T5 composite. Hence, H95T5 micropore area was higher than that of TiO_2 (3.7 and 2.1 cm^3/g, respectively). These results showed that combining HNT and TiO_2 had a strong impact on the sample microporous structure. This should be beneficial for H95T5 photocatalytic activity because it promotes adsorption, desorption and diffusion of reactants and product activity [40,45].

Table 2. BET surface and micropore area of TiO_2, HNT, and H95T5.

	Halloysite	**TiO_2**	**H95T5**
BET surface (m^2/g)	35.7	58.4	36.6
Micropore area (cm^3/g)	----------	2.1	3.7

3.2.Electrochemical activity

After confirming H95T5 structural and morphological modifications and HNT incorporation in TiO_2, the electrochemical activity was evaluated using EIS, a powerful technique for assessing the charge transfer and recombination processes at the nanofiber-electrolyte interface. It allows determining the photo-induced charge separation efficiency and transmission rate.[81,82]

The Nyquist curves showed that resistance decreased after adding TiO_2 and upon exposure to visible light radiation (**Fig. 5.a**). The model was depicted using the equivalent circuit of R_1 + *CPE*//R_2, where R_1 was the bulk resistance of electrodes and electrolyte, R_2 represented the resistance formed at the interface of the nanofibers and electrolytes, and *CPE* denoted the double layer capacitance at the nanofibers and the electrolyte interface[83]. All Nyquist plots and parameters are illustrated in **Fig. 5.b** and **Table 3.** TiO_2 displayed the fastest charge transfer rate and the best photogenerated electron-hole separation compared with the other nanofibers, as indicated by its lowest R_2 value (1136.8 Ω). The R_2 value of H95T5 (5% of TiO_2) increased to 1280 Ω. The R_2 of HNT was 6027.8 Ω, which indicates lower recombination rate between electrons and holes and thus, longer electron lifetime[57].

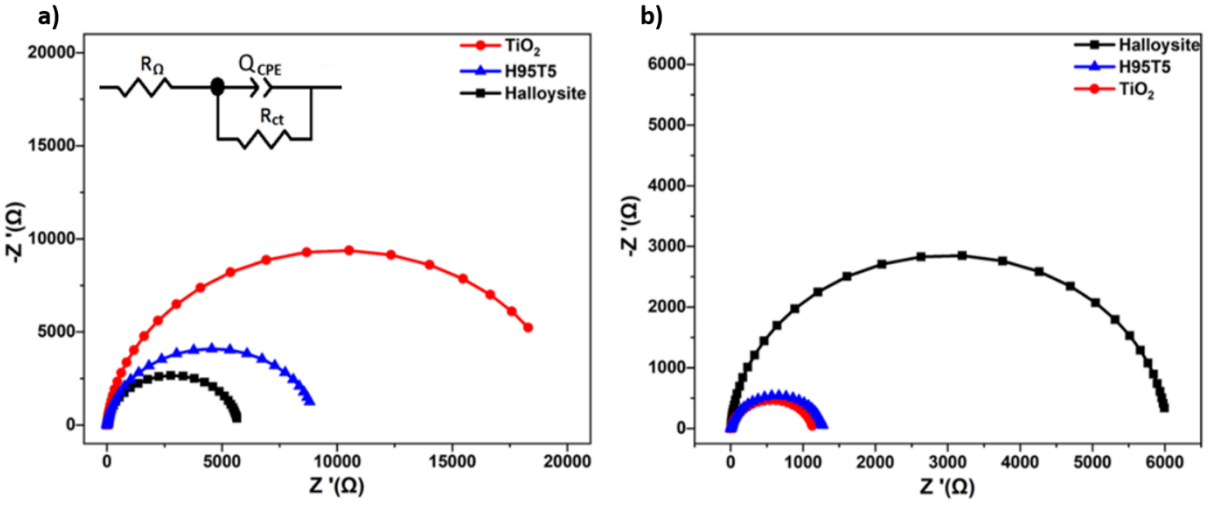

Fig. 5 The Nyquist curves (obtained by EIS) of halloysite, TiO_2 and H95T5 in the dark (a) and under visible light (b). The proposed circuit is illustrated in the inset.

Table 3. Electrochemical impedance spectroscopy parameters

Sample	R_1 (Ω)		R_2 (Ω)		R_2 - R_1	
	Dark	Visible	Dark	Visible	Dark	Visible
Halloysite	181.4	215.9	5692.2	6027.8	5510.8	5811.9
TiO_2	215.9	203.3	2023.0	1136.8	2238.9	933.5
H95T5	183.0	166.7	9124.0	1280.0	8941.0	1113.8

3.3.Photocatalytic activity

The photocatalytic activity of HNT, TiO_2 and H95T5 was evaluated by monitoring the degradation of MB and ACT under UV and visible light irradiation. MB was chosen as a representative organic pollutant. It belongs to the xanthine family, and has a maximum absorption band at 664 nm.[84–88] ACT was selected as a drug model due to its high consumption worldwide and its wide presence in natural water and wastewater[65,68,89-90]. For comparison, the photocatalytic activities of HNT, TiO_2 and H95T5 were tested in the dark. Then, upon exposure to UV light for 4 h, it was confirmed that MB was stable and did not undergo self-photolysis (**Fig. S5**) After 10 min of UV light irradiation, 97.5% and 85.1% of MB were degraded using H95T5 and TiO_2, respectively (**Fig. 6.a** degradation percentage calculated from the spectrophotometric results presented in **Fig. S7.a**). The obtained results showed that H95T5 had high photocatalytic degradation capacity. Then, to test whether H95T5 was a good catalyst also under visible light to reduce energy consumption, the same photocatalytic experiments were carried out using visible light radiation. After 2 h of visible light irradiation, 88.7% of MB was degraded in the presence of H95T5, 93.6% in the presence of TiO_2, and only 20% in the presence of HNT (**Fig. 6.b and Fig. S6**). These data indicated that the H95T5 composite (95% of natural HNT) possesses very good photocatalytic activity upon UV and also visible light irradiation. These results are very promising for developing a new type of low-cost photocatalytic material.

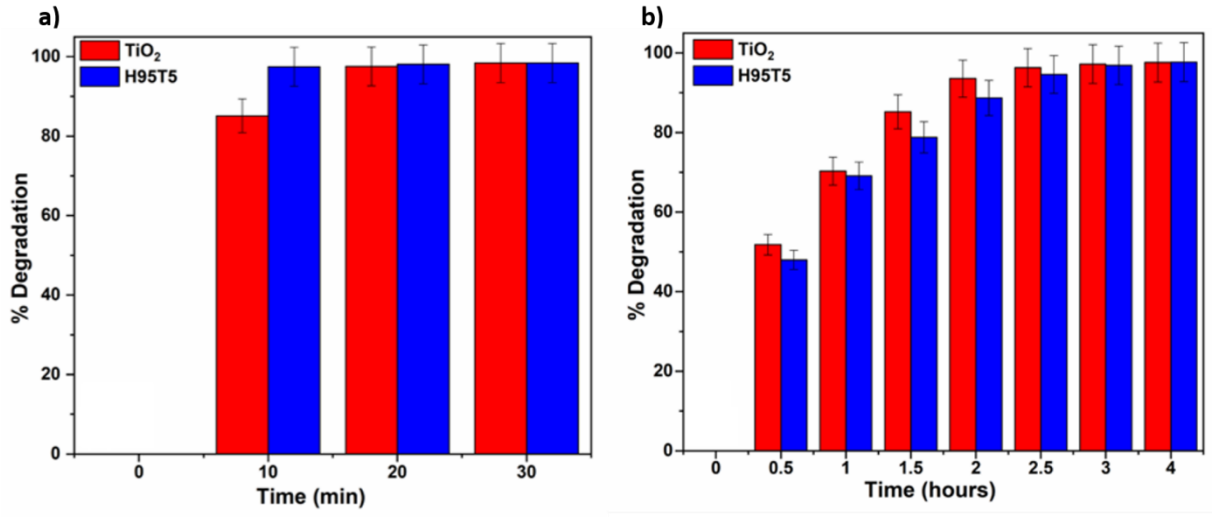

Fig. 6 Photocatalytic degradation of MB by H95T5 and TiO_2 upon exposure to UV light (a) and to visible light (b). Each measurement was performed at least three times and the relative error was lower than ±5 %.

Then, ACT degradation upon exposure to UV and visible light was monitored. After 20 min under UV irradiation, 97.5% and 85.1% of ACT were degraded in the presence of H95T5 and TiO_2, respectively (**Fig. 7.a**). ACT was completely degraded by both photocatalysts after 1 h of UV irradiation. These results confirmed that H95T5 could be used for the degradation of different pollutant types under UV irradiation with a good degradation rate. Similarly, after 6 h of visible light irradiation, 91.1% and 83.9% of ACT were degraded in the presence of H95T5 and TiO_2, respectively (**Fig. 7.b**). Then, the pollutant degradation activity of H95T5 was compared with that of other previously described photocatalysts made of HNT and TiO_2 (**Table 5**). Although it was not straightforward to compare different photocatalysts, different experimental conditions (concentration of photocatalyst and pollutants), different irradiation types, and different synthesis methods, it was clear that despite the low quantity of TiO_2 in H95T5, its ACT and MB degradation performances upon exposure to visible light and UV irradiation were excellent.

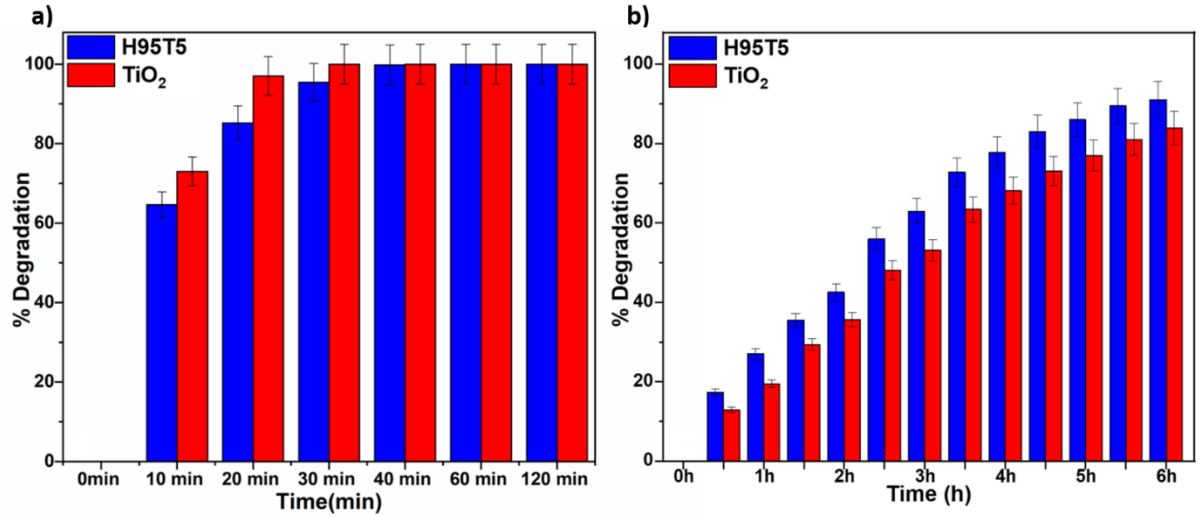

Fig. 7 Photocatalytic degradation of ACT by H95T5 and TiO_2 upon exposure to UV (a) and visible light (b). All measurements were repeated at least three times and the relative error was lower than ±5 %.

Analysis of the reaction kinetics for both pollutants showed that MB and ACT photocatalysis under UV and visible light could be explained by a pseudo first-order reaction due to the linearity of the curves and the linear coefficient R^2 near to 1 (**Fig. S8** and **Table 4).** The degradation rates for both pollutants with TiO_2 nanofibers as catalyst were higher than those of H95T5 under visible and UV lights. This demonstrated that TiO_2 nanofibers displayed the best photocatalytic activities for ACT and MB degradation, which is logical considering that H95T5 is mainly made of clay.

Table 4. ACT and MB degradation efficiency and kinetics using TiO_2 and H95T5.

Pollutant	Irradiation	Photocatalyst	Degradation (%)	K_{app} x10^{-2} (min^{-1})	Correlation coefficient R^2
ACT	UV	TiO_2	100.00	16.64	0.98
		H95T5	100.00	9.72	0.99
ACT	Visible	TiO_2	83.90	0.48	0.99
		H95T5	91.10	0.64	0.99
MB	UV	TiO_2	99.98	17.42	0.98
		H95T5	99.98	15.51	0.99
MB	Visible	TiO_2	98.40	1.87	0.97
		H95T5	96.83	1.75	0.98

As H95T5 was a good photocatalyst for MB and ACT degradation, its stability (0.5 g/l) was evaluated over five successive cycles using ACT at a concentration of 10 mg/L at pH 7. After each experiment, the photocatalyst was removed by filtration, washed with deionized water several times, and dried at 100°C for 12 h. The catalyst remained stable without loss of activity after five cycles (**Fig. 8.a**). Therefore, due to its high catalytic activity and good stability, H95T5 is a promising material for further development in catalysis.

Next, to understand the degradation mechanism, quenching tests were carried out to identify the reactive radicals responsible for ACT degradation. The photocatalysis experiments were performed as described above, but in the presence of radical scavengers (isopropanol, benzoquinone, EDTA) (**Fig. 8.b and c**). Specifically, each scavenger (0.06M[91]) was added to the ACT solution before exposure to the light source[101]. Aliquots were taken at different time points during the reaction, and ACT concentration was analyzed with the same chromatographic method as before. When isopropanol (•OH scavenger) was added, ACT degradation rate was reduced considerably. As •OH, radicals are very reactive, their reduction by the scavenger inhibited degradation, indicating that •OH radicals were involved in ACT degradation. Addition of benzoquinone, which can trap $O_2^{\bullet-}$ radicals, inhibited ACT degradation. This demonstrated the participation of $O_2^{\bullet-}$ in the photodegradation process. Addition of EDTA led to degradation inhibition by ~70%, indicating that h+ also were involved in ACT degradation[57]. Overall, these data showed that •OH, h^+ and $O_2^{\bullet-}$ radicals were the main reactive species involved in ACT photodegradation [57].

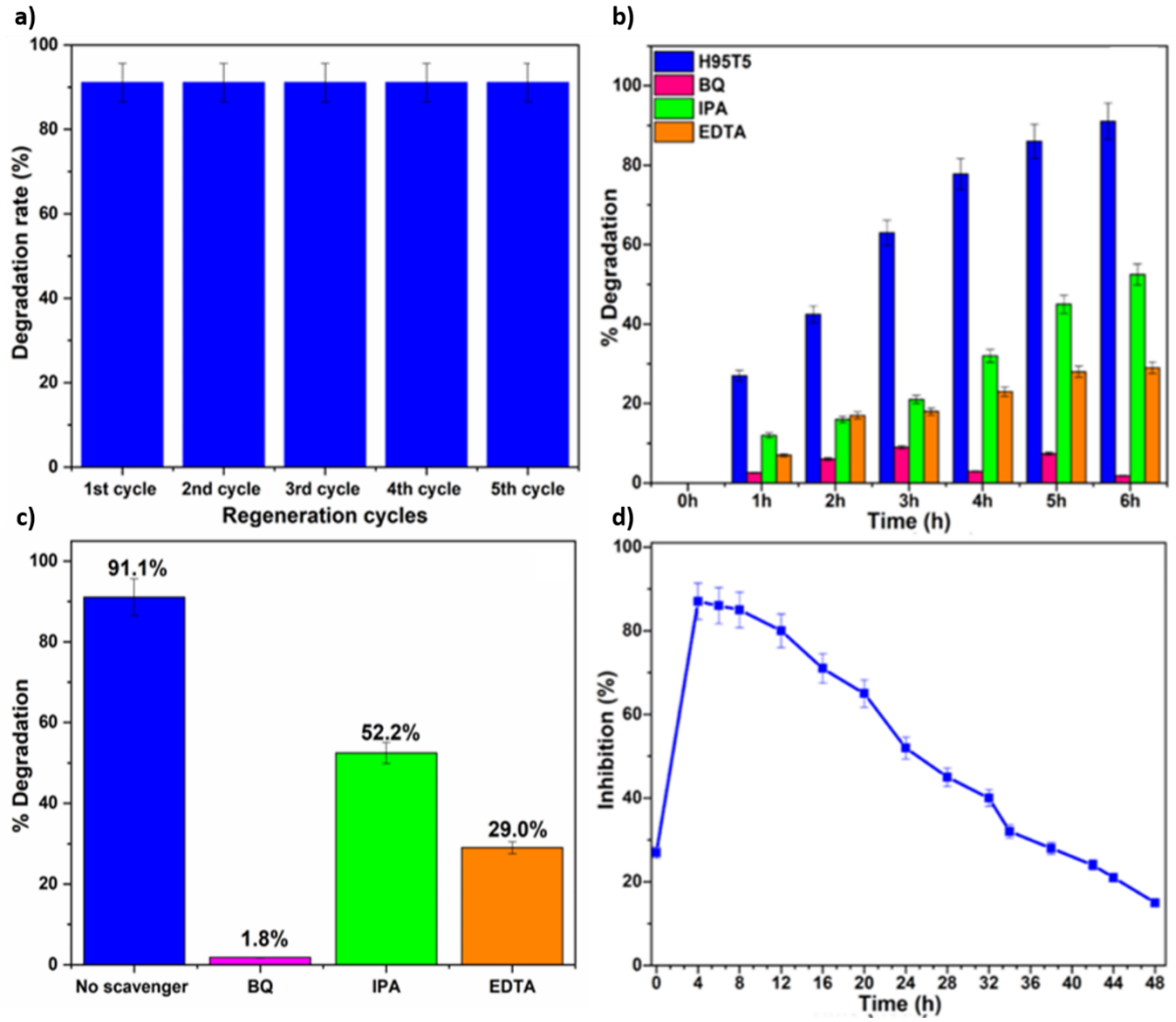

Fig. 8 Reusability of H95T5 as photocatalyst (a). Plots showing the results of the experiments with the indicated radical scavengers to identify the reactive species implicated in ACT degradation by H95T5 (b,c). Vibrio fischeri luminescence inhibition during ACT degradation by H95T5 under visible light irradiation (d). BQ: benzoquinone; IPA, isopropanol.

Lastly, bacterial toxicity tests were performed to determine whether toxic by-products were produced during ACT degradation. After 15 min of contact between *V. fischeri* and the solution of H95T5 and ACT, the percentage of bacterial luminescence inhibition by ACT was 27% and increased to 87% after 4 h of irradiation, demonstrating the formation of toxic aromatic by-products (**Fig. 8.d**). The inhibition percentage decreased slowly to 80% after 12 h, to 52% after 24 h, to 24% after 42 h, and to 15% after 48 h. This demonstrated ACT removal efficiency by H95T5 under visible light irradiation. This result is consistent with the previously demonstrated formation of toxic aromatic by-products, such as 1,4-benzoquinone, benzoic acid, and benzaldehyde, and their transformation into non-toxic compounds, such as carboxylic acids (e.g. maleic acid, oxalic acid)[51,52,94].

Table 5. Degradation efficiency of different photocatalysts (previous studies) and comparison with H95T5.

Pollutant (mg/L)	Photocatalyst (g/L)	Method	Type of irradiation	Removal efficiency (%)	Degradation time (min)	Ref
ACT (10 mg/L)	H95T5 (0.5 g/L)	Sol-gel + Electrospinning	Medium pressure metal halide UV	100	60	This work
ACT (10 mg/L)			Halogen linear lamp	91.10	360	
MB (6.64 mg/L)			Medium pressure metal halide UV	99.98	20	
MB (6.64 mg/L)			Halogen linear lamp	96.83	180	
MB 20 mg/L	TiO_2@HNT (4.2g/L)	Sol-gel + Phase inversion	125 W UV lamp (254 nm)	87.47	120	39
RB 20 mg/L				96.87	120	
MB (32 mg/L)	TiO_2/HNT (0.5 g/L)	Sol-gel	12 W UV lamp (λ= 365 nm)	81.60	240	42
Acetic acid 5 mL of 5 vol %	TiO_2/HNTs (20 mg)	Solvothermal	100 W high-pressure lamp	3488.63 µmol/g	60	40
Methanol 5 mL of 5 vol %				729.37 µmol/g	120	
Tetracycline 20 mg/L	Ce- TiO_2/HNT (0.5 g/L)	Sol-gel	300 W Xe lamp ($\lambda > 420$)	78.00	60	69
Basic Blue 41 (12 mg/L)	Ag/ TiO_2-HNT (0.625g/L)	Sol-gel	Four black light fluorescent tubes with nominal power of 4 W	100	100	95
MB (20 mg/L)	Carbon- TiO_2-HNT (8%) (0.2g/L)	Sol-gel + Electrospinning	50 W UV lamps (k < 420 nm)	81.00	90	45
4-NP (10 mg/L)	Amylose–halloysite–TiO_2 (1 g/L)	Ball milling + Sol-gel	12 W UV lamp (λ = 253 nm)	90.00	240	43
ACT (10 mg/L)	MWCNT 10%-TiO_2-SiO_2	Ultrasonic + Sol–gel	Visible irradiation high pressure mercury lamp	81.60	60	96
ACT (30 mg/L)	Fe_2O_3-TiO_2 (0.25g/L)	Sol-gel	Solar simulator halogen lamp	94.80	180	97

ACT (20 mg/L)	Degussa P25 (2g/L)	Commercial	UV irradiation 365nm	98.00	60	[98]
ACT (0.08 mg/L)	TiO_2-Ag 5% (1g/L)	Photodeposition	UV irradiation 365nm	98.00	180	[99]
ACT (20 mg/L)	Pt-TiO_2 0.4g/L	Photodeposition synthesis	Solar irradiation	100	180	[100]

4. Conclusion

TiO_2-based composite nanofibers with a large amount of HNT (95%) were successfully prepared by combining the sol-gel and electrospinning methods. The prepared catalyst was annealed at 400°C to preserve the original HNT structure. XRD and Raman spectroscopy showed that TiO_2 was well incorporated inside the nanofibers. Moreover, TEM images showed good HNT dispersion and confirmed that HNT nanotubes were located inside the TiO_2 nanofibers. Although the catalyst included only 5% of TiO_2, H95T5 efficiently degraded MB and ACT under UV (97.5% of MB after 10 min and 100% of ACT after 60 min) and visible light irradiation (97% of MB after 3 h and 91% of ACT after 6 h). In addition, H95T5 catalytic performance remained unchanged after five consecutive cycles, demonstrating its stability. The scavenging experiments revealed that $^{\bullet}OH$, h^+ and $O_2^{\bullet-}$ radicals were the main reactive species involved in ACT photodegradation. These findings suggest that this Tunisian clay is an alternative material for developing a clean, environmentally friendly, less energy-demanding, and low-cost photocatalyst for removing dyes and pharmaceuticals from wastewater, and open prospects for mass production and practical applications.

Acknowledgements

This work was funded by project H2020-MSCA-RISE-2017, 'Novel 1D photonic metal oxide nanostructures for early stage cancer detection' (Project number: 778157). I.I. acknowledges partial funding by the NCN SONATA-BIS program (UMO-2020/38/B/ST5/00176). This project received funding from the Research Council of Lithuania (LMTLT), GILIBERT 2021 program agreement No S-LZ- 21–4, and was co-funded by Campus France grant No. 46593RA (PHC GILIBERT 2021). M.A. would like to thank the Ministry of Higher Education and Scientific Research of Tunisia for financial support.

References

(1) Volkan Bozkir. A Moral Failure: Billions of People with No Access to Clean Drinking Water.

(2) Masindi, V.; Muedi, K. L. Environmental Contamination by Heavy Metals. In *Heavy Metals*; Saleh, H. E.-D. M., Aglan, R. F., Eds.; InTech, 2018. https://doi.org/10.5772/intechopen.76082.

(3) Anku, W. W.; Mamo, M. A.; Govender, P. P. Phenolic Compounds in Water: Sources, Reactivity, Toxicity and Treatment Methods. In *Phenolic Compounds - Natural Sources, Importance and Applications*; Soto-Hernández, M., Palma-Tenango, M., Garcia-Mateos, M. del R., Eds.; InTech, 2017. https://doi.org/10.5772/66927.

(4) Hussain, S.; Khan, N.; Gul, S.; Khan, S.; Khan, H. Contamination of Water Resources by Food Dyes and Its Removal Technologies. In *Water Chemistry*; Eyvaz, M., Yüksel, E., Eds.; IntechOpen, 2020. https://doi.org/10.5772/intechopen.90331.

(5) Snyder, S. A.; Westerhoff, P.; Yoon, Y.; Sedlak, D. L. Pharmaceuticals, Personal Care Products, and Endocrine Disruptors in Water: Implications for the Water Industry. *Environ. Eng. Sci.* **2003**, *20* (5), 449–469. https://doi.org/10.1089/10928750376833593 1.

(6) Stackelberg, P. E.; Gibs, J.; Furlong, E. T.; Meyer, M. T.; Zaugg, S. D.; Lippincott, R. L. Efficiency of Conventional Drinking-Water-Treatment Processes in Removal of Pharmaceuticals and Other Organic Compounds. *Sci. Total Environ.* **2007**, *377* (2–3), 255–272. https://doi.org/10.1016/j.scitotenv.2007.01.095.

(7) Stehle, S.; Schulz, R. Agricultural Insecticides Threaten Surface Waters at the Global Scale. *Proc. Natl. Acad. Sci.* **2015**, *112* (18), 5750. https://doi.org/10.1073/pnas.1500232112.

(8) Russo, V.; Hmoudah, M.; Broccoli, F.; Iesce, M. R.; Jung, O.-S.; Di Serio, M. Applications of Metal Organic Frameworks in Wastewater Treatment: A Review on Adsorption and Photodegradation. *Front. Chem. Eng.* **2020**, *2*, 15. https://doi.org/10.3389/fceng.2020.581487.

(9) Jeirani, Z.; Niu, C. H.; Soltan, J. Adsorption of Emerging Pollutants on Activated Carbon. *Rev. Chem. Eng.* **2017**, *33* (5). https://doi.org/10.1515/revce-2016-0027.

(10) Huang, Y.; Su, W.; Wang, R.; Zhao, T. Removal of Typical Industrial Gaseous Pollutants: From Carbon, Zeolite, and Metal-Organic Frameworks to Molecularly Imprinted Adsorbents. *Aerosol Air Qual. Res.* **2019**, *19* (9), 2130–2150. https://doi.org/10.4209/aaqr.2019.04.0215.

(11) Rodriguez-Narvaez, O. M.; Peralta-Hernandez, J. M.; Goonetilleke, A.; Bandala, E. R. Treatment Technologies for Emerging Contaminants in Water: A Review. *Chem. Eng. J.* **2017**, *323*, 361–380. https://doi.org/10.1016/j.cej.2017.04.106.

(12) Teodosiu, C.; Gilca, A.-F.; Barjoveanu, G.; Fiore, S. Emerging Pollutants Removal through Advanced Drinking Water Treatment: A Review on Processes and Environmental Performances Assessment. *J. Clean. Prod.* **2018**, *197*, 1210–1221. https://doi.org/10.1016/j.jclepro.2018.06.247.

(13) Use of Selected Advanced Oxidation Processes (AOPs) for Wastewater Treatment - a Mini Review. *Glob. NEST J.* **2013**, *10* (3), 376–385. https://doi.org/10.30955/gnj.000598.

(14) Paul Guin, J.; Bhardwaj, Y. K.; Varshney, L. Mineralization and Biodegradability Enhancement of Methyl Orange Dye by an Effective Advanced Oxidation Process. *Appl. Radiat. Isot.* **2017**, *122*, 153–157. https://doi.org/10.1016/j.apradiso.2017.01.018.

(15) Herrmann, J.-M. Heterogeneous Photocatalysis: Fundamentals and Applications to the Removal of Various Types of Aqueous Pollutants. *Catal. Today* **1999**, *53* (1), 115–129. https://doi.org/10.1016/S0920-5861(99)00107-8.

(16) Rauf, M. A.; Ashraf, S. S. Fundamental Principles and Application of Heterogeneous Photocatalytic Degradation of Dyes in Solution. *Chem. Eng. J.* **2009**, *151* (1–3), 10–18. https://doi.org/10.1016/j.cej.2009.02.026.

(17) Maeda, K. Photocatalytic Water Splitting Using Semiconductor Particles: History and Recent Developments. *J. Photochem. Photobiol. C Photochem. Rev.* **2011**, *12* (4), 237–268. https://doi.org/10.1016/j.jphotochemrev.2011.07.001.

(18) Bhatnagar, A.; Hogland, W.; Marques, M.; Sillanpää, M. An Overview of the Modification Methods of Activated Carbon for Its Water Treatment Applications. *Chem. Eng. J.* **2013**, *219*, 499–511. https://doi.org/10.1016/j.cej.2012.12.038.

(19) Zhao, B.; Yu, H.; Liu, Y.; Lu, Y.; Fan, W.; Qin, W.; Huo, M. Enhanced Photoelectrocatalytic Degradation of Acetaminophen Using a Bifacial Electrode of Praseodymium-Polyethylene Glycol-PbO2//Ti//TiO2-Nanotubes. *Chem. Eng. J.* **2021**, *410*, 128337. https://doi.org/10.1016/j.cej.2020.128337.

(20) Lebeau, B.; Jonas, F.; Gaudin, P.; Bonne, M.; Blin, J.-L. Dyes Depollution of Water Using Porous TiO2-Based Photocatalysts. In *Environmental Nanotechnology Volume 4*; Dasgupta, N., Ranjan, S., Lichtfouse, E., Eds.; Springer International Publishing: Cham, 2020; Vol. 32, pp 35–92. https://doi.org/10.1007/978-3-030-26668-4_2.

(21) Khaki, M. R. D.; Shafeeyan, M. S.; Raman, A. A. A.; Daud, W. M. A. W. Application of Doped Photocatalysts for Organic Pollutant Degradation - A Review. *J. Environ. Manage.* **2017**, *198*, 78–94. https://doi.org/10.1016/j.jenvman.2017.04.099.

(22) Moma, J.; Baloyi, J. Modified Titanium Dioxide for Photocatalytic Applications. In *Photocatalysts - Applications and Attributes*; Bahadar Khan, S., Akhtar, K., Eds.; IntechOpen, 2019. https://doi.org/10.5772/intechopen.79374.

(23) Coy, E.; Siuzdak, K.; Pavlenko, M.; Załęski, K.; Graniel, O.; Ziółek, M.; Balme, S.; Miele, P.; Weber, M.; Bechelany, M.; Iatsunskyi, I. Enhancing Photocatalytic Performance and Solar Absorption by Schottky Nanodiodes Heterojunctions in Mechanically Resilient Palladium Coated TiO2/Si Nanopillars by Atomic Layer Deposition. *Chem. Eng. J.* **2020**, *392*, 123702. https://doi.org/10.1016/j.cej.2019.123702.

(24) Ainali, N. M.; Kalaronis, D.; Evgenidou, E.; Bikiaris, D. N.; Lambropoulou, D. A. Insights into Biodegradable Polymer-Supported Titanium Dioxide Photocatalysts for Environmental Remediation. *Macromol* **2021**, *1* (3). https://doi.org/10.3390/macromol1030015.

(25) Ali, I.; Asim, Mohd.; Khan, T. A. Low Cost Adsorbents for the Removal of Organic Pollutants from Wastewater. *J. Environ. Manage.* **2012**, *113*, 170–183. https://doi.org/10.1016/j.jenvman.2012.08.028.

(26) Asahi, R.; Morikawa, T.; Ohwaki, T.; Aoki, K.; Taga, Y. Visible-Light Photocatalysis in Nitrogen-Doped Titanium Oxides. *Science* **2001**, *293* (5528), 269–271. https://doi.org/10.1126/science.1061051.

(27) Mills, A.; Le Hunte, S. An Overview of Semiconductor Photocatalysis. *J. Photochem. Photobiol. Chem.* **1997**, *108* (1), 1–35. https://doi.org/10.1016/S1010-6030(97)00118-4.

(28) Hernández-Alonso, M. D.; Fresno, F.; Suárez, S.; Coronado, J. M. Development of Alternative Photocatalysts to TiO2: Challenges and Opportunities. *Energy Environ. Sci.* **2009**, *2* (12), 1231. https://doi.org/10.1039/b907933e.

(29) Shan, A. Y.; Ghazi, T. I. Mohd.; Rashid, S. A. Immobilisation of Titanium Dioxide onto Supporting Materials in Heterogeneous Photocatalysis: A Review. *Appl. Catal. Gen.* **2010**, *389* (1–2), 1–8. https://doi.org/10.1016/j.apcata.2010.08.053.

(30) Rao, K. V. S.; Subrahmanyam, M.; Boule, P. Immobilized TiO2 Photocatalyst during Long-Term Use: Decrease of Its Activity. *Appl. Catal. B Environ.* **2004**, *49* (4), 239–249. https://doi.org/10.1016/j.apcatb.2003.12.017.

(31) Elgamouz, A.; Tijani, N. From a Naturally Occurring-Clay Mineral to the Production of Porous Ceramic Membranes. *Microporous Mesoporous Mater.* **2018**, *271*, 52–58. https://doi.org/10.1016/j.micromeso.2018.05.030.

(32) Manova, E.; Aranda, P.; Angeles Martín-Luengo, M.; Letaïef, S.; Ruiz-Hitzky, E. New Titania-Clay Nanostructured Porous Materials. *Microporous Mesoporous Mater.* **2010**, *131* (1–3), 252–260. https://doi.org/10.1016/j.micromeso.2009.12.031.

(33) Rainer, D. N.; Morris, R. E. New Avenues for Mechanochemistry in Zeolite Science. *Dalton Trans.* **2021**, *50* (26), 8995–9009. https://doi.org/10.1039/D1DT01440D.

(34) García-Romero, E.; Suárez, M. Sepiolite–Palygorskite: Textural Study and Genetic Considerations. *Appl. Clay Sci.* **2013**, *86*, 129–144. https://doi.org/10.1016/j.clay.2013.09.013.
(35) Ruiz-Hitzky, E.; Aranda, P.; Álvarez, A.; Santarén, J.; Esteban-Cubillo, A. Advanced Materials and New Applications of Sepiolite and Palygorskite. In *Developments in Clay Science*; Elsevier, 2011; Vol. 3, pp 393–452. https://doi.org/10.1016/B978-0-444-53607-5.00017-7.
(36) Fernandes, A. C.; Antunes, F.; Pires, J. Sepiolite Based Materials for Storage and Slow Release of Nitric Oxide. *New J. Chem.* **2013**, *37* (12), 4052. https://doi.org/10.1039/c3nj00452j.
(37) Li, R.; Li, T.; Zhou, Q. Impact of Titanium Dioxide (TiO2) Modification on Its Application to Pollution Treatment—A Review. *Catalysts* **2020**, *10* (7). https://doi.org/10.3390/catal10070804.
(38) Massaro, M.; Colletti, C. G.; Lazzara, G.; Milioto, S.; Noto, R.; Riela, S. Halloysite Nanotubes as Support for Metal-Based Catalysts. *J. Mater. Chem. A* **2017**, *5* (26), 13276–13293. https://doi.org/10.1039/C7TA02996A.
(39) Mishra, G.; Mukhopadhyay, M. TiO2 Decorated Functionalized Halloysite Nanotubes (TiO2@HNTs) and Photocatalytic PVC Membranes Synthesis, Characterization and Its Application in Water Treatment. *Sci. Rep.* **2019**, *9* (1), 4345. https://doi.org/10.1038/s41598-019-40775-4.
(40) Wang, R.; Jiang, G.; Ding, Y.; Wang, Y.; Sun, X.; Wang, X.; Chen, W. Photocatalytic Activity of Heterostructures Based on TiO_2 and Halloysite Nanotubes. *ACS Appl. Mater. Interfaces* **2011**, *3* (10), 4154–4158. https://doi.org/10.1021/am201020q.
(41) Papoulis, D.; Komarneni, S.; Panagiotaras, D.; Stathatos, E.; Toli, D.; Christoforidis, K. C.; Fernández-García, M.; Li, H.; Yin, S.; Sato, T.; Katsuki, H. Halloysite–TiO2 Nanocomposites: Synthesis, Characterization and Photocatalytic Activity. *Appl. Catal. B Environ.* **2013**, *132–133*, 416–422. https://doi.org/10.1016/j.apcatb.2012.12.012.
(42) Du, Y.; Zheng, P. Adsorption and Photodegradation of Methylene Blue on TiO2-Halloysite Adsorbents. *Korean J. Chem. Eng.* **2014**, *31* (11), 2051–2056. https://doi.org/10.1007/s11814-014-0162-8.
(43) Zheng, P.; Du, Y.; Chang, P. R.; Ma, X. Amylose–Halloysite–TiO2 Composites: Preparation, Characterization and Photodegradation. *Appl. Surf. Sci.* **2015**, *329*, 256–261. https://doi.org/10.1016/j.apsusc.2014.12.158.
(44) Moslehyani, A.; Farnood, R.; Tabe, S.; Matsuura, T.; Ismail, A. F. Novel Nanocomposite HNT-TiO2/PVDF Adsorptive Nanofiber Membranes for Arsenic (III) Removal. *J. Membr. Sci. Res.* **2020**, *6* (4), 416–423. https://doi.org/10.22079/jmsr.2020.135081.1407.
(45) Jiang, L.; Huang, Y.; Liu, T. Enhanced Visible-Light Photocatalytic Performance of Electrospun Carbon-Doped TiO2/Halloysite Nanotube Hybrid Nanofibers. *J. Colloid Interface Sci.* **2015**, *439*, 62–68. https://doi.org/10.1016/j.jcis.2014.10.026.
(46) Ben Rhaiem, H.; Tessier, D.; Ben Haj Amara, A. Mineralogy of the <2 Mm Fraction of Three Mixed-Layer Clays from Southern and Central Tunisia. *Clay Miner.* **2000**, *35* (2), 375–381. https://doi.org/10.1180/000985500546846.
(47) Abi Younes, P.; Sayegh, S.; Nada, A. A.; Weber, M.; Iatsunskyi, I.; Coy, E.; Abboud, N.; Bechelany, M. Elaboration of Porous Alumina Nanofibers by Electrospinning and Molecular Layer Deposition for Organic Pollutant Removal. *Colloids Surf. Physicochem. Eng. Asp.* **2021**, *628*, 127274. https://doi.org/10.1016/j.colsurfa.2021.127274.
(48) Najem, M.; Nada, A. A.; Weber, M.; Sayegh, S.; Razzouk, A.; Salameh, C.; Eid, C.; Bechelany, M. Palladium/Carbon Nanofibers by Combining Atomic Layer Deposition and Electrospinning for Organic Pollutant Degradation. *Materials* **2020**, *13* (8), 1947. https://doi.org/10.3390/ma13081947.
(49) Kawrani, S.; Nada, A. A.; Bekheet, M. F.; Boulos, M.; Viter, R.; Roualdes, S.; Miele, P.; Cornu, D.; Bechelany, M. Enhancement of Calcium Copper Titanium Oxide Photoelectrochemical Performance Using Boron Nitride Nanosheets. *Chem. Eng. J.* **2020**, *389*, 124326. https://doi.org/10.1016/j.cej.2020.124326.

(50) Martins, P.; Kappert, S.; Nga Le, H.; Sebastian, V.; Kühn, K.; Alves, M.; Pereira, L.; Cuniberti, G.; Melle-Franco, M.; Lanceros-Méndez, S. Enhanced Photocatalytic Activity of Au/TiO2 Nanoparticles against Ciprofloxacin. *Catalysts* **2020**, *10* (2), 234. https://doi.org/10.3390/catal10020234.

(51) Konstantinou, I. Photocatalytic Transformation of Pesticides in Aqueous Titanium Dioxide Suspensions Using Artificial and Solar Light: Intermediates and Degradation Pathways. *Appl. Catal. B Environ.* **2003**, *42* (4), 319–335. https://doi.org/10.1016/S0926-3373(02)00266-7.

(52) Le, T. X. H.; Nguyen, T. V.; Amadou Yacouba, Z.; Zoungrana, L.; Avril, F.; Nguyen, D. L.; Petit, E.; Mendret, J.; Bonniol, V.; Bechelany, M.; Lacour, S.; Lesage, G.; Cretin, M. Correlation between Degradation Pathway and Toxicity of Acetaminophen and Its By-Products by Using the Electro-Fenton Process in Aqueous Media. *Chemosphere* **2017**, *172*, 1–9. https://doi.org/10.1016/j.chemosphere.2016.12.060.

(53) Fu, Y.; Wang, W.; Zhang, L.; Vinokurov, V.; Stavitskaya, A.; Lvov, Y. Development of Marine Antifouling Epoxy Coating Enhanced with Clay Nanotubes. *Materials* **2019**, *12* (24), 4195. https://doi.org/10.3390/ma12244195.

(54) Cheng, R.; Li, H.; Liu, Z.; Du, C. Halloysite Nanotubes as an Effective and Recyclable Adsorbent for Removal of Low-Concentration Antibiotics Ciprofloxacin. *Minerals* **2018**, *8* (9), 387. https://doi.org/10.3390/min8090387.

(55) Saif, M. J.; Asif, H. M.; Naveed, M. PROPERTIES AND MODIFICATION METHODS OF HALLOYSITE NANOTUBES: A STATE-OF-THE-ART REVIEW. *J. Chil. Chem. Soc.* **2018**, *63* (3), 4109–4125. https://doi.org/10.4067/s0717-97072018000304109.

(56) Pan, Q.; Li, N.; Hong, Y.; Tang, H.; Zheng, Z.; Weng, S.; Zheng, Y.; Huang, L. Halloysite Clay Nanotubes as Effective Nanocarriers for the Adsorption and Loading of Vancomycin for Sustained Release. *RSC Adv.* **2017**, *7* (34), 21352–21359. https://doi.org/10.1039/C7RA00376E.

(57) Sayegh, S.; Tanos, F.; Nada, A.; Lesage, G.; Zaviska, F.; Petit, E.; rouessac, vincent; yatsunskiy, igor; Coy, E.; Viter, R.; damberga, daina; Weber, M.; Razzouk, A.; Stephan, J.; Bechelany, M. Tunable TiO2-BN-Pd Nanofibers by Combining Electrospinning and Atomic Layer Deposition to Enhance Photodegradation of Acetaminophen. *Dalton Trans.* **2022**, 10.1039.D1DT03715C. https://doi.org/10.1039/D1DT03715C.

(58) Orlando, J. D.; Limbu, T. B.; Chitara, B.; Yan, F. One-Pot Electronspinning of Polyvinylpyrrolidone/Cellulose Acetate/TiO2 Nanofibrous Membranes with Enhanced Photocatalytic Properties. *J. Porous Mater.* **2020**, *27* (3), 911–918. https://doi.org/10.1007/s10934-020-00866-4.

(59) Albetran, H.; Dong, Y.; Low, I. M. Characterization and Optimization of Electrospun TiO_2 /PVP Nanofibers Using Taguchi Design of Experiment Method. *J. Asian Ceram. Soc.* **2015**, *3* (3), 292–300. https://doi.org/10.1016/j.jascer.2015.05.001.

(60) Kuchi, C.; Reddy, P. S. Effect of Polymer Concentration and Annealing Temperature on TiO2-PVP Composite Nanofiber Mats Prepared with Homemade Electrospinning; Bikaner, India, 2018; p 030241. https://doi.org/10.1063/1.5032576.

(61) Nasr, M.; Balme, S.; Eid, C.; Habchi, R.; Miele, P.; Bechelany, M. Enhanced Visible-Light Photocatalytic Performance of Electrospun RGO/TiO_2 Composite Nanofibers. *J. Phys. Chem. C* **2017**, *121* (1), 261–269. https://doi.org/10.1021/acs.jpcc.6b08840.

(62) Bac, B. H.; Dung, N. T. Finding Nanotubular Halloysite at Lang Dong Kaolin Deposit, Phu Tho Province. *VIETNAM J. EARTH Sci.* **2016**, *37* (4), 299–306. https://doi.org/10.15625/0866-7187/37/4/8058.

(63) Bumajdad, A.; Madkour, M.; Abdel-Moneam, Y.; El-Kemary, M. Nanostructured Mesoporous Au/TiO2 for Photocatalytic Degradation of a Textile Dye: The Effect of Size Similarity of the Deposited Au with That of TiO2 Pores. *J. Mater. Sci.* **2014**, *49* (4), 1743–1754. https://doi.org/10.1007/s10853-013-7861-0.

(64) Addamo, M.; Bellardita, M.; Di Paola, A.; Palmisano, L. Preparation and Photoactivity of Nanostructured Anatase, Rutile and Brookite TiO2 Thin Films. *Chem. Commun.* **2006**, No. 47, 4943. https://doi.org/10.1039/b612172a.

(65) Papoulis, D.; Panagiotaras, D.; Tsigrou, P.; Christoforidis, K. C.; Petit, C.; Apostolopoulou, A.; Stathatos, E.; Komarneni, S.; Koukouvelas, I. Halloysite and Sepiolite –TiO2 Nanocomposites: Synthesis Characterization and Photocatalytic Activity in Three Aquatic Wastes. *Mater. Sci. Semicond. Process.* **2018**, *85*, 1–8. https://doi.org/10.1016/j.mssp.2018.05.025.

(66) Nyankson, E.; Kumar, R. V. Removal of Water-Soluble Dyes and Pharmaceutical Wastes by Combining the Photocatalytic Properties of Ag3PO4 with the Adsorption Properties of Halloysite Nanotubes. *Mater. Today Adv.* **2019**, *4*, 100025. https://doi.org/10.1016/j.mtadv.2019.100025.

(67) Ibrahim, E. E.; Chipara, D. M.; Thapa, R.; Lozano, K.; Chipara, M. Raman Spectroscopy of Isotactic Polypropylene-Halloysite Nanocomposites. *J. Nanomater.* **2012**, *2012*, 1–8. https://doi.org/10.1155/2012/793084.

(68) Zhang, Q.; Ma, L.; Shao, M.; Huang, J.; Ding, M.; Deng, X.; Wei, X.; Xu, X. Anodic Oxidation Synthesis of One-Dimensional TiO_2 Nanostructures for Photocatalytic and Field Emission Properties. *J. Nanomater.* **2014**, *2014*, 1–14. https://doi.org/10.1155/2014/831752.

(69) Wang, H.; Wu, D.; Li, X.; Huo, P. Ce Doping TiO2/Halloysite Nanotubes Photocatalyst for Enhanced Electrons Transfer and Photocatalytic Degradation of Tetracycline. *J. Mater. Sci. Mater. Electron.* **2019**, *30* (21), 19126–19136. https://doi.org/10.1007/s10854-019-02268-y.

(70) Cavallaro, G.; Danilushkina, A.; Evtugyn, V.; Lazzara, G.; Milioto, S.; Parisi, F.; Rozhina, E.; Fakhrullin, R. Halloysite Nanotubes: Controlled Access and Release by Smart Gates. *Nanomaterials* **2017**, *7* (8), 199. https://doi.org/10.3390/nano7080199.

(71) Dhal, J. P.; Sahoo, S. K.; Padhiari, S.; Dash, T.; Hota, G. In-Situ Synthesis of Mixed Phase Electrospun TiO2 Nanofibers: A Novel Visible Light Photocatalyst. *SN Appl. Sci.* **2019**, *1* (3), 243. https://doi.org/10.1007/s42452-019-0261-6.

(72) Massaro, M.; Colletti, C. G.; Guernelli, S.; Lazzara, G.; Liu, M.; Nicotra, G.; Noto, R.; Parisi, F.; Pibiri, I.; Spinella, C.; Riela, S. Photoluminescent Hybrid Nanomaterials from Modified Halloysite Nanotubes. *J. Mater. Chem. C* **2018**, *6* (27), 7377–7384. https://doi.org/10.1039/C8TC01424H.

(73) Cheng, Z.-L.; Sun, W. Preparation and Solar Light Photocatalytic Activity of N-Doped TiO2-Loaded Halloysite Nanotubes Nanocomposites. *J. Mater. Eng. Perform.* **2015**, *24* (10), 4090–4095. https://doi.org/10.1007/s11665-015-1699-3.

(74) Sing, K. The Use of Nitrogen Adsorption for the Characterisation of Porous Materials. *Colloids Surf. Physicochem. Eng. Asp.* **2001**, *187–188*, 3–9. https://doi.org/10.1016/S0927-7757(01)00612-4.

(75) ALOthman, Z. A Review: Fundamental Aspects of Silicate Mesoporous Materials. *Materials* **2012**, *5* (12), 2874–2902. https://doi.org/10.3390/ma5122874.

(76) Filippo, E.; Capodilupo, A. L.; Carlucci, C.; Perulli, P.; Conciauro, F.; Corrente, G. A.; Scremin, B. F.; Gigli, G.; Ciccarella, G. Efficient, Green Non-Aqueous Microwave-Assisted Synthesis of Anatase TiO_2 and Pt Loaded TiO_2 Nanorods with High Photocatalytic Performance. *Nanomater. Nanotechnol.* **2015**, *5*, 31. https://doi.org/10.5772/61147.

(77) Li, X.; Zou, M.; Wang, Y. Soft-Template Synthesis of Mesoporous Anatase TiO2 Nanospheres and Its Enhanced Photoactivity. *Molecules* **2017**, *22* (11), 1943. https://doi.org/10.3390/molecules22111943.

(78) Liu, F.; Yan, X.; Chen, X.; Tian, L.; Xia, Q.; Chen, X. Mesoporous TiO2 Nanoparticles Terminated with Carbonate-like Groups: Amorphous/Crystalline Structure and Visible-Light Photocatalytic Activity. *Catal. Today* **2016**, *264*, 243–249. https://doi.org/10.1016/j.cattod.2015.07.012.

(79) Yao, P.; Zhong, S.; Shen, Z. TiO_2 /Halloysite Composites Codoped with Carbon and Nitrogen from Melamine and Their Enhanced Solar-Light-Driven Photocatalytic Performance. *Int. J. Photoenergy* **2015**, *2015*, 1–8. https://doi.org/10.1155/2015/605690.

(80) Szczepanik, B.; Słomkiewicz, P.; Garnuszek, M.; Rogala, P.; Banaś, D.; Kubala-Kukuś, A.; Stabrawa, I. Effect of Temperature on Halloysite Acid Treatment for Efficient Chloroaniline Removal from Aqueous Solutions. *Clays Clay Miner.* **2017**, *65* (3), 155–167. https://doi.org/10.1346/CCMN.2017.064056.

(81) Sacco, A. Electrochemical Impedance Spectroscopy: Fundamentals and Application in Dye-Sensitized Solar Cells. *Renew. Sustain. Energy Rev.* **2017**, *79*, 814–829. https://doi.org/10.1016/j.rser.2017.05.159.

(82) Herrera Hernández, H.; M. Ruiz Reynoso, A.; C. Trinidad González, J.; O. González Morán, C.; G. Miranda Hernández, J.; Mandujano Ruiz, A.; Morales Hernández, J.; Orozco Cruz, R. Electrochemical Impedance Spectroscopy (EIS): A Review Study of Basic Aspects of the Corrosion Mechanism Applied to Steels. In *Electrochemical Impedance Spectroscopy*; El-Azazy, M., Min, M., Annus, P., Eds.; IntechOpen, 2020. https://doi.org/10.5772/intechopen.94470.

(83) Djara, R.; Lacour, M.-A.; Merzouki, A.; Cambedouzou, J.; Cornu, D.; Tingry, S.; Holade, Y. Iridium and Ruthenium Modified Polyaniline Polymer Leads to Nanostructured Electrocatalysts with High Performance Regarding Water Splitting. *Polymers* **2021**, *13* (2), 190. https://doi.org/10.3390/polym13020190.

(84) Shimizu, N.; Ogino, C.; Dadjour, M. F.; Murata, T. Sonocatalytic Degradation of Methylene Blue with TiO2 Pellets in Water. *Ultrason. Sonochem.* **2007**, *14* (2), 184–190. https://doi.org/10.1016/j.ultsonch.2006.04.002.

(85) Gorduk, S.; Avciata, O.; Avciata, U. Photocatalytic Degradation of Methylene Blue under Visible Light Irradiation by Non-Peripherally Tetra Substituted Phthalocyanine-TiO2 Nanocomposites. *Inorganica Chim. Acta* **2018**, *471*, 137–147. https://doi.org/10.1016/j.ica.2017.11.004.

(86) Dariani, R. S.; Esmaeili, A.; Mortezaali, A.; Dehghanpour, S. Photocatalytic Reaction and Degradation of Methylene Blue on TiO2 Nano-Sized Particles. *Optik* **2016**, *127* (18), 7143–7154. https://doi.org/10.1016/j.ijleo.2016.04.026.

(87) Gupta, V. K.; Jain, R.; Mittal, A.; Saleh, T. A.; Nayak, A.; Agarwal, S.; Sikarwar, S. Photo-Catalytic Degradation of Toxic Dye Amaranth on TiO2/UV in Aqueous Suspensions. *Mater. Sci. Eng. C* **2012**, *32* (1), 12–17. https://doi.org/10.1016/j.msec.2011.08.018.

(88) Jing, H.-P.; Wang, C.-C.; Zhang, Y.-W.; Wang, P.; Li, R. Photocatalytic Degradation of Methylene Blue in ZIF-8. *RSC Adv* **2014**, *4* (97), 54454–54462. https://doi.org/10.1039/C4RA08820D.

(89) Danfá, S.; Martins, R. C.; Quina, M. J.; Gomes, J. Supported TiO2 in Ceramic Materials for the Photocatalytic Degradation of Contaminants of Emerging Concern in Liquid Effluents: A Review. *Molecules* **2021**, *26* (17), 5363. https://doi.org/10.3390/molecules26175363.

(90) Fischer, K.; Grimm, M.; Meyers, J.; Dietrich, C.; Gläser, R.; Schulze, A. Photoactive Microfiltration Membranes via Directed Synthesis of TiO2 Nanoparticles on the Polymer Surface for Removal of Drugs from Water. *J. Membr. Sci.* **2015**, *478*, 49–57. https://doi.org/10.1016/j.memsci.2015.01.009.

(91) Gómez-Avilés, A.; Peñas-Garzón, M.; Bedia, J.; Rodriguez, J. J.; Belver, C. C-Modified TiO2 Using Lignin as Carbon Precursor for the Solar Photocatalytic Degradation of Acetaminophen. *Chem. Eng. J.* **2019**, *358*, 1574–1582. https://doi.org/10.1016/j.cej.2018.10.154.

(92) Du, J.; Zhang, J.; Yang, T.; Liu, R.; Li, Z.; Wang, D.; Zhou, T.; Liu, Y.; Liu, C.; Che, G. The Research on the Construction and the Photocatalytic Performance of BiOI/NH2-MIL-125(Ti) Composite. *Catalysts* **2020**, *11* (1), 24. https://doi.org/10.3390/catal11010024.

(93) Zheng, X.; Yuan, J.; Shen, J.; Liang, J.; Che, J.; Tang, B.; He, G.; Chen, H. A Carnation-like RGO/Bi2O2CO3/BiOCl Composite: Efficient Photocatalyst for the Degradation of Ciprofloxacin. *J. Mater. Sci. Mater. Electron.* **2019**, *30* (6), 5986–5994. https://doi.org/10.1007/s10854-019-00898-w.

(94) Konstantinou, I. K.; Albanis, T. A. TiO2-Assisted Photocatalytic Degradation of Azo Dyes in Aqueous Solution: Kinetic and Mechanistic Investigations. *Appl. Catal. B Environ.* **2004**, *49* (1), 1–14. https://doi.org/10.1016/j.apcatb.2003.11.010.

(95) Nanocrystalline TiO2 and Halloysite Clay Mineral Composite Films Prepared by Sol-Gel Method: Synergistic Effect and the Case of Silver Modification to the Photocatalytic Degradation of Basic Blue- 41 Azo Dye in Water. *Glob. NEST J.* **2014**, *16* (3), 485–498. https://doi.org/10.30955/gnj.001323.

(96) Czech, B.; Tyszczuk-Rotko, K. Visible-Light-Driven Photocatalytic Removal of Acetaminophen from Water Using a Novel MWCNT-TiO2-SiO2 Photocatalysts. *Sep. Purif. Technol.* **2018**, *206*, 343–355. https://doi.org/10.1016/j.seppur.2018.06.025.

(97) Khasawneh, O. F. S.; Palaniandy, P.; Ahmadipour, M.; Mohammadi, H.; Bin Hamdan, M. R. Removal of Acetaminophen Using Fe2O3-TiO2 Nanocomposites by Photocatalysis under Simulated Solar Irradiation: Optimization Study. *J. Environ. Chem. Eng.* **2021**, *9* (1), 104921. https://doi.org/10.1016/j.jece.2020.104921.

(98) Aguilar, C. A.; Montalvo, C.; Ceron, J. G.; Moctezuma, E. Photocatalytic Degradation of Acetaminophen. *Int. J. Environ. Res.* **2011**, *5* (4). https://doi.org/10.22059/ijer.2011.465.

(99) Aguilar, C. A.; Montalvo, C.; Zermeño, B. B.; Cerón, R. M.; Cerón, J. G.; Anguebes, F.; Ramírez, M. A. Photocatalytic Degradation of Acetaminophen, Tergitol and Nonylphenol with Catalysts TiO2/Ag under UV and Vis Light. *Int. J. Environ. Sci. Technol.* **2019**, *16* (2), 843–852. https://doi.org/10.1007/s13762-018-1707-x.

(100) Nasr, O.; Mohamed, O.; Al-Shirbini, A.-S.; Abdel-Wahab, A.-M. Photocatalytic Degradation of Acetaminophen over Ag, Au and Pt Loaded TiO2 Using Solar Light. *J. Photochem. Photobiol. Chem.* **2019**, *374*, 185–193. https://doi.org/10.1016/j.jphotochem.2019.01.032.